Journal of Applied Fluid Mechanics, Vol. 13, No. 3, pp. 1015-1026, 2020.
Available online at www.jafmonline.net, ISSN 1735-3572, EISSN 1735-3645.
DOI: 10.29252/jafm.13.03.30800

Analytical Solutions for Unsteady Pipe Flows with Slip Boundary Condition

Anek. V. Pillai and K. V. Manu†

Department of Aerospace Engineering, Indian Institute of Space Science and Technology, Thiruvananthapuram 695547, Kerala, India

†*Corresponding Author Email: manukv@iist.ac.in*

(Received July 25, 2019; accepted September 17, 2019)

ABSTRACT

In this paper analytical expressions for time-dependent velocity profiles and pressure gradient are obtained for fully-developed laminar flows with given volume flow-rate conditions in circular pipe flows with slip boundary conditions. The governing equations are solved analytically using the traditional Laplace transform method together with Mellin's inversion formula. The evolution of velocity profiles and pressure gradient for starting and pulsatile flow with slip boundary conditions are analyzed. New simplified expressions and perspectives on velocity and pressure gradient for no-slip and slip flows are obtained from the analytical results. New scalings in starting and pulsatile flows are proposed for pipe flows with no-slip and slip boundary conditions using non-dimensional numbers. Special attention is paid to the effect of slip factor and pulsatile flow frequency on the time-dependent skin-friction factor. Finally, by using the starting and pulsating flow results, analytical expressions of velocity and pressure for arbitrary inflow are obtained by approximating the arbitrary volume flow-rate by a Fourier series

Keywords: Micropipe; Starting flow; Pulsatile flow; Womersley number.

NOMENCLATURE

c	non-dimensional length-scale ratio
C_f	friction coefficient
Kn	Knudsen number
L	mean free path of gas molecule
p	pressure
r	radial distance from center of pipe
R	radius of the pipe
Re	Reynolds number
t	time
T	non-dimensional time scale for oscillatory flows
u	axial component of velocity in pipe
u_{avg}	average velocity of axial velocity
u_c	axial velocity at the center of the pipe
u_r	radial velocity component
u_θ	circumferential velocity component
U	velocity scale
U_0	axial velocity for starting flows
U_c	axial velocity for cosine flows
U_s	axial velocity for sine flows
W_o	square of Womersley number
x	axial distance of the pipe
x^*	non-dimensional axial distance of the pipe
α	Womersley number
β	viscous slip coefficient
η	navier length
ν	kinematic viscosity
ρ	density of the fluid
τ	non-dimensional time scale for starting flows
ω	angular frequency of oscillation

1 I|NTRODUCTION

The scientific and practical interest to micro-pipe flows has constantly increased over the past few years. Micro-energy systems and micro-electromechanical systems are few of the well-known applications. One of the most useful and well-known applications is the efficient cooling of chips using micro heat pipes. Besides these, they have also found applications in bio-engineering systems. Recent experimental studies at nano and micro level have shown that the frequently used no-slip condition can conditionally breakdown, depending

on the interfacial interaction between the fluid and solid surfaces. In such cases, the boundary condition can drastically differ from the no-slip boundary condition. Aforesaid, boundary condition can commonly arise from rarefaction effect and superhydrophobicity.

It has been observed that for Knudsen number (Kn = λ/D, where λ is the mean free path and D is the characteristic length) in the range of $10^{-2} \leq Kn \leq 10^{-1}$, the flow is essentially governed by Navier-Stokes equation with slip flow boundary condition. Because of wide modern potential applications in micro and nano-fluidic systems, the slip boundary condition has regained attention from the fluid mechanics community. Therefore it is of utmost importance to gain a clear understanding of flow behavior with slip boundary conditions.

The concept of partial-slip boundary condition is as old as the Navier-Stokes equation itself. Navier, in the middle of the nineteenth century, posited a Robin boundary condition by relating the wall-velocity to the shear-rate at the wall. In Navier's model, the velocity at the solid boundary (slip velocity) varies linearly with the magnitude of flow shear-rate at the wall as follows:

$$u_{wall} = \eta \left| \frac{\partial u}{\partial y}_{wall} \right|, \tag{1}$$

Where η is the 'Navier-length' (commonly called as slip-length) defined as the distance into the wall at which the fluid velocity extrapolates to zero. Maxwell rigorously quantified slip-length for gases flowing over a solid wall and the value was found to be of the order of mean free path of the fluid. The commonly used no-slip and perfect-slip conditions are cases with proportionality constant values equal to zero and infinity respectively.

Over the past two decades, the theory of starting and pulsating flows with no-slip boundary conditions has been a subject of intense research and the theory of time-dependent laminar flows has been well documented in books by Batchelor (Batchelor, 1967), Schlichting and Gersten (2016) and Jog (2002). The first mathematical solution of unidirectional unsteady flow was given by Stokes using similarity method by solving the diffusion equation during the course of study of pendulum friction (Panton, 2013). In Stokes' study, the pressure upstream and downstream of the solid surface is kept constant during the motion. Rayleigh illustrated the boundary layer character of the Stokes flow and creatively used the analytical solution of Stokes to derive an approximate expression for skin-friction on a finite length flat-plate. The essence of Rayleigh argument was the idea of replacing the time scale with $\mathcal{L}$ /U, where $\mathcal{L}$ is the distance from the leading edge. Further mathematical extension of the Stokes problem is the pressure gradient-driven starting flows in long pipes and channels. In such cases, the expression for velocity and pressure are generally represented by Fourier/Bessel series.

Two types of procedures are commonly used for obtaining the analytical solutions for laminar, fully-developed pulsatory flows with constant properties. In the first category (Fourier transform approach), the pressure gradient variation is normally assumed a waveform, rep-resented by Fourier series (Womersley, 1955; Uchida, 1956; Khan, 2007; Majdalani, 2008; Hayat *et al.* 2010). The most influential studies and widely cited works related to the first approach are the pipe flow solutions of Womersley (1955) and Uchida (1956). Majdalani (2008) extended the method proposed by Uchida (1956) to channel flows with no slip boundary condition. Recently, Ray *et al.* (2005) obtained the analytical solution for different types of pulsation by approximating the mass flow-rate by Fourier series. In the second category (Laplace transform approach (Das & Arakeri, 2000; Brereton, 2000; Muntges & Majdalani, 2002; Khaled & Vafai, 2004; Chen *et al*., 2008; Hayat *et al*., 2011; Avramenko *et al.,* 2015), the pressure gradient is an unknown parameter and the additional condition to solve the governing equation is obtained from the time-varying mean volume flow-rate.

Das and Arakeri (2000) successfully applied the second method to obtain the transient variation of the velocity profile and pressure gradient for different in-flow configurations. Muntges and Majdalani (2002) extended the method suggested by Das and Arakeri (2000) for an arbitrary volume flow-rate in channel flows. In an interesting study, (Brereton (2000) obtained the analytical relation between flow-rate, pressure gradient and wall friction for arbitrary inflow using Laplace transform methods for channel and pipe flows.

Chen *et al*. (2008) have used the method suggested by Das and Arakeri (2000) to circular pipes with slip boundary conditions for trapezoidal and starting flows. Using Laplace transform method Khaled and Vafai (2004) obtained an exact analytical solutions of Stokes and Couette flows commenced by sinusoidal motion of a wall with slip boundary conditions. Recently, many works have been devoted to study the effect of dynamic slip boundary condition (Kaoullas & Georgiou, 2013; *Damianou et al*., 2014; Kaoullas & Georgiou, 2015) (where the slip velocity is a function of previous wall shear stress state) on pressure gradient and velocity profiles in different flows configurations.

In an interesting study Avramenko *et al.,* 2015) obtained an analytical solution for starting flows with slip conditions for pipe and channel flows. To model the starting flow, Avramenko *et al.* (2015) represented the pressure gradient term using a Heaviside function and solved using Cauchy's residue theorem in conjunction with the Laplace transform method. In this work we have considered three unsteady flows in a pipe with known inlet flow-rate (Q (t)) variation than the pressure gradient variation which is considered in many other previous studies. Defining known time varying volume rate at the inlet instead of pressure gradient is beneficial in flow conditions where pressure is more laborious to measure than volume flow rate. Also, from practical point of view, known inlet flow-rate conditions are more frequently encountered than the pressure gradient variation. Here, the transient behavior of

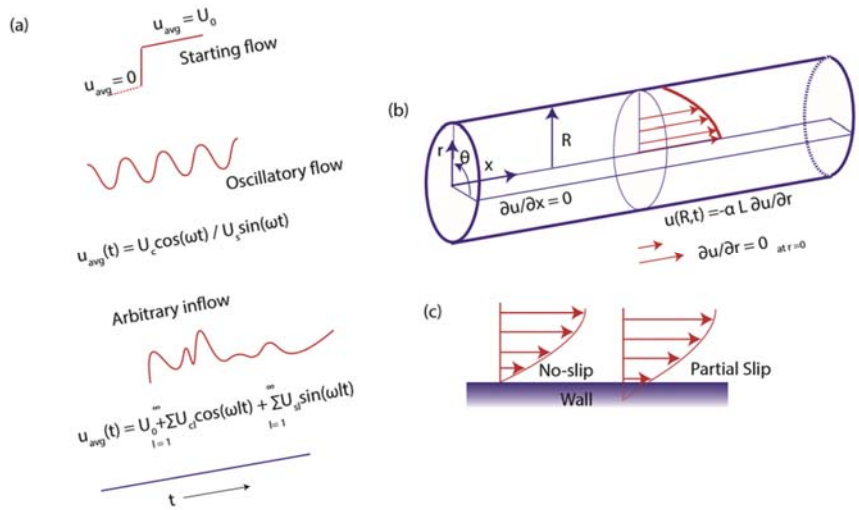

Fig. 1. Schematic depiction of the investigated flow-configurations with boundary conditions.

velocity and pressure gradient in pipe flows with slip conditions for starting, oscillatory and arbitrary inflows are analytically investigated. We use the classical Laplace transform method to obtain the explicit expressions between the flow variables. Due to the captivating applications of hydrophobic surfaces associated with the drag reduction, special attention is given to the skin-friction factor.

This paper is organized as follows. The mathematical details used for solving the governing equations are mentioned in section 2. Solutions to starting, pulsating and arbitrary flows are also provided in section 2. The results obtained in section 2 are analyzed in section 3 where the temporal variation of velocity, pressure gradient, skin-friction factor and asymptotic nature of the solution for starting and oscillatory flow are analyzed. The results are summarized in section 4.

2. MATHEMATICAL FORMULATION

A sketch of the unidirectional flow through pipe along with the coordinate system employed for the present study is shown in Fig. 1. We consider incompressible fluid through a pipe (Fig. 1 (b)) with radius R. The density, dynamic and kinematic viscosities are represented using the symbols ρ, μ and ν respectively. Using cylindrical coordinates, (r, θ, x), where r = 0 is the axis of the pipe and u_r, u_θ and u are the velocities in r, θ, and x directions respectively. We have considered three unsteady flow cases (starting, oscillatory and arbitrary) with known inlet volume rate as shown in Fig. 1 (a). For starting flow the fluid is initially at rest and brought into motion at t = 0 in such a way that the velocity suddenly jumps to a constant value. The inlet flow conditions for starting flow are:

$$u_{avg}(t) = 0 \text{ for } t \le 0, \quad (2)$$
$$= U_0 \text{ for } t > 0.$$

For oscillatory flow the mean inlet velocity is represented by sine or cosine function. The inlet flow conditions for single-frequency oscillatory flows starting from rest are as follows:

$$u_{avg}(t) = 0 \text{ for } t \le 0, \quad (3)$$
$$= U_c \cos\omega t \text{ for } t > 0 \text{ (for cosine flows)},$$
$$= U_s \sin\omega t \text{ for } t > 0 \text{ (for sine flows)}.$$

Here, u_{avg} is the mean velocity at the inlet of the pipe and ω is the angular frequency of the oscillation. In arbitrary flow case, the mean inlet velocity is varied randomly with flow time. To represent a general arbitrary inflow, the mean velocity profile is approximated by a Fourier series. The arbitrary flow consists of mean and fluctuating components as follows:

$$u_{avg}(t) = U_0 + \sum_{l=1}^{\infty} U_{cl}\cos(lwt) + \sum_{l=1}^{\infty} U_{cl}\sin(lwt) \quad (4)$$

The partial slip flow boundary conditions is imposed at the wall (Fig. 1 (c)).

For analyzing the analytical expressions for pressure and velocity profiles for starting, oscillatory and arbitrary flows with slip boundary conditions, non-dimensional numbers are defined in the following way. The non-dimensional length-scale ratios are defined as:

$$c = \frac{r}{R} \quad (5)$$

$$x^* = \frac{x}{R} \quad (6)$$

The non-dimensional time scales are defined as:

$$\tau = \frac{\nu t}{R^2} \quad (7)$$

$$T = wt \quad (8)$$

Inertia and viscous forces are compared using Reynolds number (Re) and Womersley number (α). The square of Womersley number is represented using the symbol W_o.

$$Re = \frac{2UR}{v} \tag{9}$$

$$\alpha = R\sqrt{\frac{w}{v}} \tag{10}$$

$$W_0 = \frac{wR^2}{v} \tag{11}$$

Here, U is the velocity scale. The velocity scale for the starting flow is U_0 and for oscillatory flow, the amplitude of the wave (U_c and Us for cosine and sine flows respectively) is used.

The non-dimensional pressure, pressure gradient, Knudsen number and friction factor are defined as:

$$p^* = \frac{p}{8\mu U/R} \tag{12}$$

$$\frac{dp^*}{dx^*} = \left(\frac{R^2}{8\mu U}\right)\frac{dp}{dx} \tag{13}$$

$$Kn = \frac{\beta L}{R} \tag{14}$$

$$C_f = -\frac{\mu\frac{\partial u}{\partial y}_{wall}}{\frac{1}{2}\rho U^2} \tag{15}$$

Here β is the viscous slip coefficient and L is the mean free path of a gas molecule.

2.1 Solution of the Governing Equation

Here, we consider incompressible, fully-developed transient flow with constant thermo-physical properties in an infinitely long circular pipe with zero swirl ($u_r = u_\theta = 0$).

In the absence of body forces, the momentum equation in the cylindrical coordinate system reduces to:

$$\frac{\partial u}{\partial t} = -\frac{1}{\rho}\frac{\partial p}{\partial x} + \nu\left(\frac{\partial^2 u}{\partial r^2} + \frac{1}{r}\frac{\partial u}{\partial r}\right) \tag{16}$$

The boundary conditions are as follows:

$$u(r,0) = 0,\ \ u(R,t) = -\beta L\frac{\partial u}{\partial r}\ \ and \frac{\partial u(0.t)}{\partial r} = 0 \tag{17}$$

$$\int_0^R 2\pi u(r,t)\,dr = u_{avg}(t)\pi R^2 = Q(t) \tag{18}$$

Taking the Laplace transform of the governing equation (Eq. 16) and the boundary conditions (Eqs. 17 and 18) yield:

$$\frac{d^2\bar{u}(r,s)}{dr^2} + \frac{1}{r}\frac{d\bar{u}(r,s)}{dr} - \frac{s}{\nu}\bar{u}(r,s) = \frac{1}{\mu}\frac{d\bar{p}}{dx} - \frac{1}{\nu}\bar{u}(r,0) \tag{19}$$

$$\bar{u}(R,s) = - - \beta L\frac{\partial\bar{u}(R,s)}{\partial r},$$
$$\frac{\partial\bar{u}(0,s)}{\partial r} = 0, \qquad and$$
$$\int_0^R 2\pi r\bar{u}\,dr = \bar{u}_{avg}(s)\pi R^2.$$

By applying the transformed boundary conditions, the solution of the subsidiary governing equation is obtained as follows:

$$\bar{u}(r,s) = u_{avg}(s).\bar{\xi}(r,s) \tag{20}$$

where,

$$\bar{\xi}(r,s) = \frac{I_0(B\sqrt{s}) + Kn(B\sqrt{s})I_1(B\sqrt{s}) - I_0(A\sqrt{s})}{I_0(B\sqrt{s}) + Kn(B\sqrt{s})I_1(B\sqrt{s}) - \frac{2I_1(B\sqrt{s})}{B\sqrt{s}}}$$

The inverse Laplace transform is calculated using Mellin's inverse formula.

$$u(r,t) = \frac{1}{2\pi i}\int_{\gamma-i\omega}^{\gamma+i\omega}\bar{u}_{avg}(s)\,\bar{\xi}(r,s)e^{st}ds \tag{21}$$

The above complex integral is evaluated using the Cauchy residue theorem.

The pressure gradient obtained from the Eqs. 19 and 20 is written as follows,

$$\frac{d\bar{p}}{dx} = \frac{-s\rho\bar{u}_{avg}(s)[I_0(B\sqrt{s}) + Kn(B\sqrt{s})I_1(B\sqrt{s})]}{I_0(B\sqrt{s}) + Kn(B\sqrt{s})I_1(B\sqrt{s}) - \frac{2I_1(B\sqrt{s})}{B\sqrt{s}}} \tag{22}$$

The time-varying pressure gradient is obtained by taking the inverse Laplace transform of Eq. 22.

2.2 Starting Flows

By taking the Laplace transform of Eq. 2 and substituting into Eq. 21, followed by the inverse Laplace transform and simplification (the derivation is described briefly in the Appendix), the solution for the velocity profiles are given by:

$$\frac{u(r)}{U_0} = 2\left[\frac{(1-c^2)+2Kn}{1+4Kn}\right] + 2\sum_{n=1}^{\infty}e^{-\nu_n^2\tau}\mathfrak{B}(\nu, \mathrm{Kn}, \mathrm{r}). \tag{23}$$

where,

$$\mathfrak{B}(\nu, \mathrm{Kn}, \mathrm{r}) = \left[\frac{J_0(c\nu_n) + Kn\nu_n J_1(\nu_n) - J_0(\nu_n)}{(1+2Kn)\nu_n J_1(\nu_n) + Kn\nu_n^2 J_0(\nu_n)}\right] \tag{24}$$

here, ν_n, n = 1,2,3...,∞ are the zeros of $Kn\nu J_1(\nu) + J_2(\nu) = 0$. J_0, J_1 and J_2 denote Bessel functions of the first kind, of order zero, one and two respectively.

The analytical expressions for pressure gradient are obtained by taking the Laplace transform of Eq. 2 and substituting into Eqs. 22, followed by the inverse Laplace transform. After simplification the solutions yield:

$$\frac{dp^*}{dx^*} = -\frac{1}{1+4Kn} + \frac{1}{4}\sum_{n=1}^{\infty}e^{-\nu_n^2\tau}\mathcal{N}(\nu, \mathrm{Kn}). \tag{25}$$

where,

$$\mathcal{N}(\nu, \mathrm{Kn}) = \left[\frac{\nu_n(\nu_n Kn J_1(\nu_n) - J_0(\nu_n))}{(1+2Kn)J_1(\nu_n) + \nu_n Kn J_0(\nu_n)}\right] \tag{26}$$

2.3 Oscillatory Flows

The solution for velocity profiles are calculated by taking the Laplace transform of Eq. 3 and substituting into Eq. 21, followed by the inverse Laplace transform calculation. After simplification, the velocity profiles for the cosine flow are as follows:

$$\frac{u(r)}{U_c} = \Re\left[e^{i\omega t}\mathcal{G}(\alpha, Kn, r) + 2\sum_{n=1}^{\infty}\frac{\nu_n^4}{\nu_n^4 + W_0^2}e^{-\nu_m^2\tau}\mathfrak{B}(\nu, \mathrm{Kn}, \mathrm{r})\right] \tag{27}$$

Here $\nu_a = \alpha_l^{\frac{3}{2}}$ and α is the Womersley number. For sinusoidally varying mean flow, the velocity profiles yield (the derivation is described briefly in the Appendix):

$$\frac{u(r)}{U_c} = \Re\left[-ie^{i\omega t}\mathcal{g}(\alpha, Kn, r) + 2\sum_{n=1}^{\infty}\frac{\nu_n^2 W_0}{\nu_n^4+W_0^2}e^{-\nu_n^2\tau}\mathfrak{B}(\nu, \mathrm{Kn}, \mathrm{r})\right] \quad (28)$$

$$\mathcal{g}(\alpha, \mathrm{Kn}, \mathrm{r}) = \left[\frac{J_0(c\nu_n)+Kn\nu_a J_1(\nu_a)-J_0(\nu_a)}{J_2(\nu_a)+Kn\nu_a J_1(\nu_a)}\right] \quad (29)$$

The analytical expressions for pressure gradient are obtained by taking the Laplace transform of Eq. 3 and substituting into Eq. 22, followed by the inverse Laplace transform calculation. After simplification, the solutions for pressure gradient for cosine flow yield as follows:

$$\left(\frac{dp^*}{dx^*}\right)_c = \left[\Re\left[\frac{iW_0}{8}e^{i\omega t}Q(\alpha, Kn) + \frac{1}{4}\sum_{n=1}^{\infty}\frac{\nu_n^4}{\nu_n^4+W_0^2}e^{-\nu_n^2\tau}\mathcal{N}(\nu, \mathrm{Kn})\right]\right] \quad (30)$$

For sinusoidally varying mean flow, the expressions for pressure gradient are:

$$\left(\frac{dp^*}{dx^*}\right)_s = \Re\left[\frac{W_0}{8}e^{i\omega t}Q(\alpha, Kn) - \frac{1}{4}\sum_{n=1}^{\infty}\frac{\nu_{nW_0}^2}{\nu_n^4+W_0^2}e^{-\nu_m^2\tau}\mathcal{N}(\nu, \mathrm{Kn})\right] \quad (31)$$

where,

$$Q(\alpha, \mathrm{Kn}) = \left[\frac{J_0(\nu_a)-Kn\nu_a J_1(\nu_a)}{J_2(\nu_a)+Kn\nu_a J_1(\nu_a)}\right] \quad (32)$$

2.4 Arbitrary Flows

The solution for velocity profiles for arbitrary flow is calculated by taking the Laplace transform of Eq. 4 and substituting into Eq. 21, followed by the inverse Laplace transform calculation. The complete solution is obtained by adding the solutions of mean, cosine and sine terms. The solutions of the mean component are given by:

$$u_1(r) = U_0\left[2\left(\frac{(1-c^2)+2Kn}{1+4Kn}\right)+2\sum_{n=1}^{\infty}e^{-\nu_n^2\tau}\mathfrak{B}(\nu, \mathrm{Kn}, \mathrm{r})\right] \quad (33)$$

$$\left(\frac{dp_1^*}{dx^*}\right)_p = \left(\frac{U_0}{U_{rms}}\right)\left[-\frac{1}{1+4Kn}+\frac{1}{4}\sum_{n=1}^{\infty}e^{-\nu_n^2\tau}\mathcal{N}(\nu, \mathrm{Kn})\right] \quad (34)$$

These solutions are same as the starting flow solutions derived in the previous section (Eqs. 23, 25).

The solutions for velocity for cosine and sine flows are:

$$u_2(r) = \Re\sum_{n=1}^{\infty}U_{cl}\ \left[e^{il\omega t}\mathcal{g}(\alpha, Kn, r) + 2\sum_{n=1}^{\infty}\frac{\nu_n^4}{\nu_n^4+l^2W_0^2}e^{-\nu_n^2\tau}\mathfrak{B}(\nu, \mathrm{Kn}, \mathrm{r})\ \right] \quad (35)$$

$$u_3(r) = \Re\sum_{l=1}^{\infty}U_{sl}\ \left[-ie^{il\omega t}\mathcal{g}(\alpha, Kn, r) - 2\sum_{n=1}^{\infty}\frac{\nu_n^2 lW_0}{\nu_n^4+l^2W_0^2}e^{-\nu_n^2\tau}\mathfrak{B}(\nu, \mathrm{Kn}, \mathrm{r})\ \right] \quad (36)$$

The multiple frequency solutions for cosine and sine flows in equations are the linear summation of the single-frequency solutions derived in the previous section (Eqs. 27 and 28).

The solutions for pressure gradient for cosine and sine flows are:

$$\left(\frac{dp_2^*}{dx^*}\right)_c = \Re\sum_{l=1}^{\infty}\left(\frac{U_{cl}}{U_{rms}}\right)\times\left[\frac{ilW_0}{8}e^{il\omega t}Q(\alpha, Kn) + \frac{1}{4}\sum_{n=1}^{\infty}\frac{\nu_n^4}{\nu_n^4+l^2W_0^2}e^{-\nu_n^2\tau}\mathcal{N}(\nu, \mathrm{Kn})\right] \quad (37)$$

$$\left(\frac{dp_3^*}{dx^*}\right)_s = \Re\sum_{l=1}^{\infty}\left(\frac{U_{sl}}{U_{rms}}\right)\times\left[\frac{lW_0}{8}e^{il\omega t}Q(\alpha, Kn) - \frac{1}{4}\sum_{n=1}^{\infty}\frac{\nu_n^2 lW_0}{\nu_n^4+l^2W_0^2}e^{-\nu_n^2\tau}\mathcal{N}(\nu, \mathrm{Kn})\right] \quad (38)$$

where U_{rms} is the root mean square of the amplitudes of mean, cosine and sine functions defined as:

$$U_{rms} = \sqrt{\frac{U_0^2+\sum_{l=1}^{\infty}U_{cl}^2+\sum_{l=1}^{\infty}U_{sl}^2}{2l_{max}+1}} \quad (39)$$

Here, l_{max} is the number of Fourier coefficients used for representing the arbitrary inflow. The complete solution is obtained by:

$$u(r) = u_1(r) + u_2(r) + u_3(r), \quad (40)$$

$$\frac{dp^*}{dx^*} = \frac{dp_1^*}{dx^*}+\frac{dp_2^*}{dx^*}+\frac{dp_3^*}{dx^*} \quad (41)$$

3.1 Starting Flow: Temporal Variation of Velocity Profiles, Skin-Friction Factor and Pressure Gradient

The velocity distribution derived for starting flows (Eq. 23) has steady (first term) and transient parts (second term). The steady-state velocity profiles vary quadratically with wall normal distance**.**

The evolution of the transient part of the velocity profiles with flow-time (τ = 0.05, 0.1, 0.2 and 0.3) for two Knudsen numbers (Kn = 0 and 0.1) are shown in Fig. 2. The transient part of the velocity profiles are positive in the near-wall region and negative at the center of the geometry. For Kn = 0 (no-slip boundary condition), the velocity distribution (Figs. 2 (a) and (b)) is similar to that of the suddenly blocked flow solution derived by Weinbaum and Parker (Weinbaum and Parker (1975)). The transient velocity profiles decay with flow-time and flow reaches the steady-state as τ approaches 0.3. Hence, the steady-state solutions with slip boundary conditions are as follows(for $\tau \geq 0.3$):

$$\frac{u(r)}{U_0} = 2\left[\frac{(1-c^2)+2Kn}{1+4Kn}\right] \quad (42)$$

The steady-state center velocity (u_c) is obtained by substituting c = 0 respectively. The expressions obtained are:

$$\frac{u_c}{U_0} = 2\left[\frac{1+2Kn}{1+4Kn}\right] \quad (43)$$

The steady-state wall velocity (u_{wall}) is obtained by substituting c = 1. The expressions obtained are:

$$\left(\frac{u_{wall}}{U_0}\right) = \left[\frac{4Kn}{1+4Kn}\right] \quad (44)$$

The evolution of velocity profiles for Kn = 0.05 are shown in Figs. 3 (a) and (b). Velocity is non-dimensionalized using information from the steady-state solution. Due to the decaying nature of the transient part, the center velocity increases with flow-time as shown in Fig. 3. The velocity profile

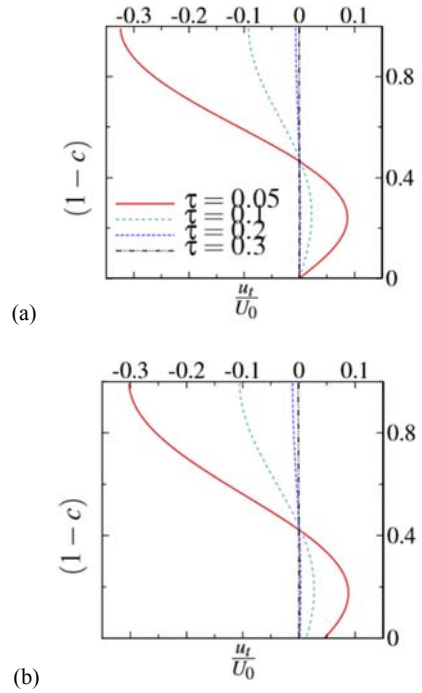

Fig. 2. Evolution of transient part of the velocity; (a) Kn = 0 (b) Kn = 0.1.

attains steady-state at $\tau \approx 0.3$. At τ equals to 0.3, the velocity profiles become parabolic. It is interesting to note that velocity profiles become independent of Knudsen number at location c $=\frac{1}{\sqrt{2}}$. Comparison between the velocity profiles for different Knudsen numbers at $\tau = 0.1$ is shown in Fig. 3 (b). A fair collapse of velocity profiles is observed near the wall proximity even at $\tau = 0.1$. At later flow-time ($\tau \geq 0.2$), all cases collapse into a single parabolic curve. In order to get further insight into the development of the velocity profile, the temporal variation of boundary layer thickness (δ) is plotted as shown in Fig. 4. Here, boundary layer thickness is defined as the distance away from the wall at which velocity is 99 percent of center velocity. Boundary layer thickness increases with increase in flow-time as shown in Fig. 4. The value of δ is lower for slip flows compared with no-slip conditions.

The steady-state expressions for velocity profiles (Eq. 42) are used to calculate the steady-state skin-friction factor (C_f). The expression obtained is:

$$C_f = \frac{16}{Re(1+4Kn)} \tag{45}$$

This equation (Eq. 45) is same as the expression obtained by Avramenko *et al.* (2015), Eq. (87)) for the limiting value of skin-friction factor.

Fig. 5 shows the temporal variation of the center velocity and skin-friction factor for four different Knudsen numbers (Kn = 0, 0.01, 0.05 and 0.1). The center velocity increases with flow-time as shown in Fig. 5 (a). Center velocity attains a constant value at $\tau \approx 0.2$.

Temporal variation of the skin-friction factor with flow-time is shown in Fig. 5 (b). The skin-friction factor is highest during the starting time, decreases with flow-time and eventually attains a constant value at $\tau \approx 0.2$. In Fig. 5 (b), the temporal variation of skin-friction factor is similar to the spatial variation at the entrance of the pipe flows.

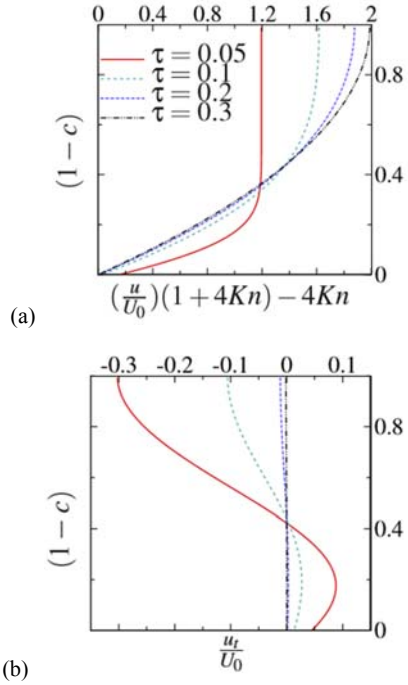

Fig. 3. (a) Velocity profiles at different flow-time at Kn = 0.05, (b) Velocity profiles for different Kn values at τ = 0.1.

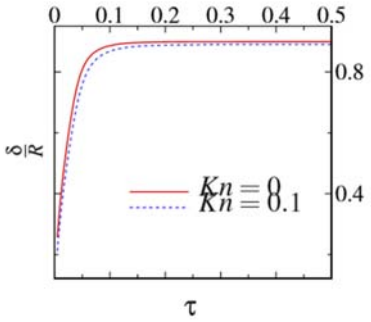

Fig. 4. Temporal variation of boundary layer thickness.

We now seek to calculate the hydrodynamic entry-length (L_h), using Rayleigh argument, by replacing the t by L_h/U_0. Since skin-friction factor attains a constant value at $\tau \approx 0.2$, we write:

$$\frac{\nu L_h}{U_0 R^2} \approx 0.2 \tag{46}$$

$$\frac{L_h}{2R} \approx 0.05Re \tag{47}$$

This is near to the experimentally observed hydrodynamic entry-length value (Durst *et al.* 2005).

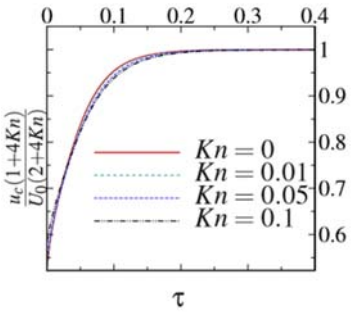

(a)

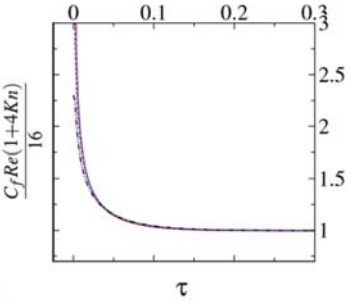

(b)

Fig. 5. (a) Temporal variation of center velocity; (b) Temporal variation of skin-friction factor.

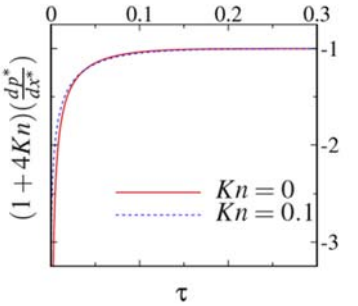

Fig. 6. Temporal variation of non-dimensional pressure gradient.

Temporal variation of pressure gradients is shown in Fig. 6. The pressure drop is highest at the begining of the flow. Pressure gradient attains a steady- state value at $\tau \approx 0.2$. The steady-state value is:

$$\left(\frac{dp^*}{dx^*}\right) = -\frac{1}{(1+4Kn)} \tag{48}$$

Furthermore, by combining the Eqs. 42 and 48, expressions for velocity profiles in terms of pressure gradient are obtained as follows:

$$u(r) = -\frac{R^2}{4\mu}\frac{dp}{dx}(1 - c^2 + Kn) \tag{49}$$

3.2 Oscillatory flows: Temporal Variation of Velocity Profiles, Skin-Friction Factor and Pressure Gradient

The velocity distribution derived for single-frequency oscillatory flows (Eqs. 27 and 28) consist of an oscillatory part (first term) and decaying part (second term). As in the starting flows, the contribution from the second term to the total velocity is negligible at $\tau \approx 0.3$. Hence for $\tau \geq 0.3$,

$$\frac{u}{U_c} = \Re\left[e^{i\omega t}\mathcal{g}(\alpha, Kn, r)\right] \tag{50}$$

$$= \cos(\omega t)\Re[\mathcal{g}(\alpha, Kn, r)] - \sin(\omega t)\Im[\mathcal{g}(\alpha, Kn, r)]$$

$$\frac{u}{U_s} = \Re\left[-ie^{i\omega t}\mathcal{g}(\alpha, Kn, r)\right] \tag{51}$$

$$= \sin(\omega t)\Re[\mathcal{g}(\alpha, Kn, r)] + \cos(\omega t)\Im[\mathcal{g}(\alpha, Kn, r)]$$

The spatial variation of real and imaginary values of $\mathcal{g}$ with Womersley number for Kn = 0 and 0.1 are shown in Figs. 7 and 8 respectively. Here, the real part profiles of G are the velocity profiles for cosine flows, when cos(ωt) = 1 (T = 2π,4π,...) and for sine flows, when sin(ωt) = 1 (T = $\frac{\pi}{2}$, $\frac{5\pi}{2}$,...).

The imaginary part profiles of $\mathcal{g}$ are the velocity profile for cosine flows, when sin(ωt) = −1 (T = $\frac{3\pi}{2}$, $\frac{7\pi}{2}$,...). and for sine flows when cos(ωt) =1(T = 2π,4π,...)

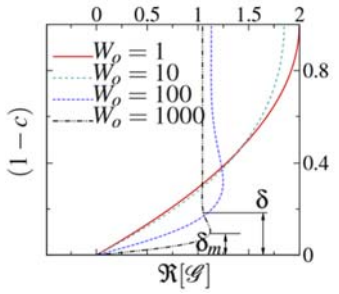

(a)

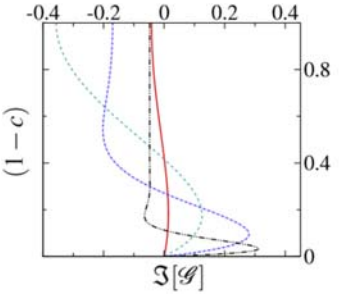

(b)

Fig. 7. Spatial variation of the real and imaginary part of $\mathcal{g}$ with Womersley number for Kn = 0.

For no-slip flows (Kn = 0), at low-Womersley numbers, the real part of $\mathcal{g}$ varies parabolically with radius. At low-Womersley number, the viscous force completely dominates the flow and the profiles are similar to the steady-state solution (Hagen-Poiseuille solution). With an increase in Womersley number, the real part of $\mathcal{g}$ profile gets flattened as shown in Fig. 7 (a). At high-Womersley number, inertia force dominates at the central core region, whereas the viscous force dominates near the wall proximity. The value at the center of the pipe approaches unity as $W_o \rightarrow \infty$. The spatial variation of imaginary values of is shown in Figs. 7 (b). Similar to the real part, the profiles get flattened with an increase in Womersley number. The value of the imaginary part of G at the center of the pipe approaches zero as $W_o \rightarrow \infty$.

Similar to the Kn = 0 case, the value of the real part

profiles of $\mathcal{g}$ at the center of the pipe decreases with increase in Womersley number for Kn = 0.1(Fig. 8 (a)). However, here, the value on the wall increases with Womersley number and both the center and wall values approach unity as $W_o \rightarrow \infty$. The spatial variation of the imaginary part for Kn = 0.1 case is shown in Fig. 8 (b). At low-Womersley number, the levels remain small. At relatively high-Womersley number, the values of the imaginary part of $\mathcal{g}$ are high near the wall proximity.

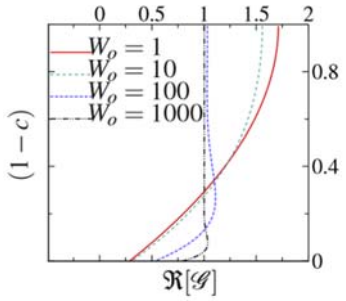

(a)

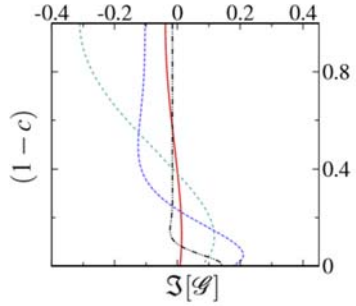

(b)

Fig. 8. Spatial variation of the real and imaginary part of $\mathcal{g}$ with Womersley number for Kn = 0.1.

At low-Womersley number, the maximum velocity is observed at the center of the pipe. With an increase in Womersley number, the maximum velocity location moves towards the wall as shown in Fig. 7. Here, the distance from the wall where the magnitude of velocity is maximum is denoted by the symbol δ_m (see Fig. 7 (a)). The variation of δ_m with Womersley number is shown in Fig. 9. Depending on the value of δ_m, the flow has been classified into low-Womersley number region (I), medium-Womersley number region (II) and high-Womersley number region (III) as shown in Fig. 9. For high-Womersley number cases, setting inertia and viscous forces equal to each other at the location δ_m yields:

$$u\omega \approx \nu \frac{u}{\delta^2} \tag{52}$$

$$\frac{\delta_m}{R} = \frac{C_{Kn}}{\alpha} \tag{53}$$

where C_{Kn} is a function of Knudsen number. Here, the values of C_{Kn}=0 and C_{Kn}=0.1 are approximately 3.24 and 2.63 respectively. At high-Womersley number cases, $\delta_m \propto \frac{1}{\alpha}$ as shown in Fig. 9.

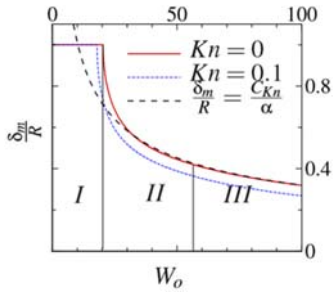

Fig. 9. Variation of δ_m with Womersley number for Kn = 0 and 0.1.

The value of function $\mathcal{g}$ at the center of the pipe are obtained in the following form by substituting c = 0 Respectively:

$$\mathcal{g}(\alpha, Kn, r=0) = \left(\frac{1+Kn\nu_a J_1(\nu_a) - J_0(\nu_a)}{J_2(\nu_a) + Kn\nu_a J_1(\nu_a)}\right) \tag{54}$$

The variation of $\mathcal{g}$ (α,Kn,r = 0) with the Womersley number for Kn = 0 and 0.1 is shown in Fig. 10 respectively. The value of the functions at Kn = 0.1 always lies below the Kn = 0 curve. The limiting value of functions $\mathcal{g}$ (α,Kn,r) as Womersley number approaches zero is calculated and obtained as follows:

$$\lim_{\alpha \to 0} \mathcal{g}\ (\mathrm{Kn}, \mathrm{r}) = 2\left[\frac{(1-c^2)+2Kn}{1+4Kn}\right] \tag{55}$$

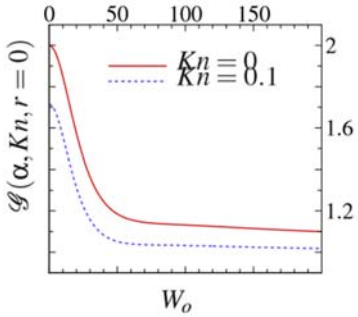

Fig. 10. G (α,Kn,r = 0) as functions of Womersley number for Kn = 0 and 0.1.

This value is same as the steady-state velocity solution obtained in the previous section (Eq. 42).

The instantaneous skin-friction factor is (for τ > 0.3):

$$C_{fc} = \Re\left[e^{i\omega t}\frac{4}{Re}\frac{\nu_a J_1(\nu_a)}{(J_2(\nu_a) + Kn\nu_a J_1(\nu_a))}\right]$$

$$C_{fs} = \Re\left[-e^{i\omega t}\frac{4}{Re}\frac{\nu_a J_1(\nu_a)}{(J_2(\nu_a) + Kn\nu_a J_1(\nu_a))}\right] \tag{56}$$

The lower limiting value of skin-friction factor is:

$$\lim_{\alpha \to 0} C_{fc} = \lim_{\alpha \to 0} C_{fs} = \frac{16}{Re(1+4Kn)}$$

The variation of the skin-friction factor of sine flow at T = $\frac{\pi}{2}$ with Womersley number is shown in Fig.11 As expected, the C_f value for slip flow (Kn = 0.1) is less than that in no-slip conditions (Kn = 0). At low-Womersley number, the value is equal to the steady-state solution. The skin-friction factor increases with an increase in Womersley number.

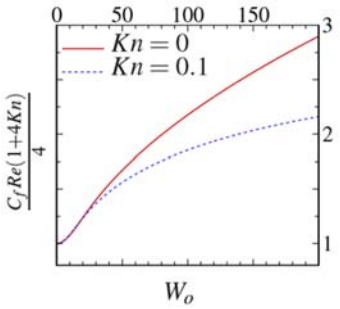

Fig. 11. Variation of skin-friction with W_o for Kn = 0 and Kn = 0.1 at T = $\frac{\pi}{2}$ for sine flow.

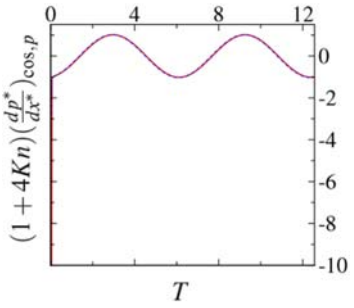

(a)

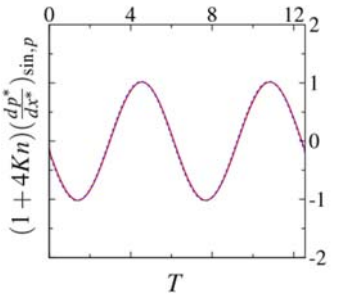

(b)

Fig. 12. Temporal variations of non-dimensional pressure gradient; (a) cosine flow (b) sine flow.

The evolution of non-dimensional pressure gradients for cosine flows for W_o = 1 is shown in Fig. 12 (a). A large pressure drop is observed at the beginning of the flow. A phase-lag between the pressure gradient and flow velocity, analogous to the voltage and current in a capacitor involving AC circuit is also observed. The evolution of non-dimensional pressure gradient for sine flows is shown in Fig. 12 (b). Unlike the cosine flow, here the flow evolves smoothly from rest and exhibits pure oscillatory behavior from the beginning itself. The expressions for pressure gradient for cosine flow (for $\tau > 0.3$) are

$$\left(\frac{dp^*}{dx^*}\right)_c = \Re\left[\frac{iW_0}{8} e^{i\omega t} Q(\alpha, Kn)\right] \tag{57}$$

$$= \frac{W_0}{8} [-\sin(\omega t)\Re[Q(\alpha, Kn)] - \cos(\omega t)\Im[Q(\alpha, Kn)]]$$

The expressions for pressure gradient for sine flow are:

$$\left(\frac{dp^*}{dx^*}\right)_s = \Re\left[\frac{W_0}{8} e^{i\omega t} Q(\alpha, Kn)\right] \tag{58}$$

$$= \frac{W_0}{8} [\cos(\omega t)\Re[Q(\alpha, Kn)] - \sin(\omega t)\Im[Q(\alpha, Kn)]]$$

Furthermore, the expressions for velocity profiles in terms of pressure gradient are obtained in the following form:

$$u(r) = \frac{i}{\omega\rho}\left(\frac{dp}{dx}\right)\left[1 - \frac{J_0(cv_a)}{J_0(v_a) - Knv_a J_1(v_a)}\right] \tag{59}$$

3.2.1 Low-Womersley Number Flows

An ascending series solution of velocity profiles for low-Womersley number flows in terms of trigonometric functions and W_o is obtained in the following way.

$$\left(\frac{J_0(cv_a) + Knv_a J_1(v_a) - J_0(v_a)}{J_2(v_a) + Knv_a J_1(v_a)}\right) = a_0 + a_1 v_a^2 + O[v_a]^3$$

Where,

$$a_0 = \frac{2(1-c^2) + 4Kn}{1 + 4Kn}$$

$$a_1 = \frac{3c^4(1+4Kn) - 4c^2(1+6Kn) + (1+8Kn)}{24(1+4Kn)^2}$$

$$\frac{u}{U_c} = a_0 \cos(\omega t) + W_0 a_1 \sin(\omega t) \tag{60}$$

$$\frac{u}{U_s} = a_0 \sin(\omega t) - W_0 a_1 \cos(\omega t) \tag{61}$$

For $W_o < 1$, the center (c = 0) and wall velocity (c = 1) are:

$$\frac{u_c}{U_c} \approx \left(\frac{4Kn+2}{4Kn+1}\right) cos(\omega t) \tag{62}$$

$$\frac{u_c}{U_s} \approx \left(\frac{4Kn+2}{4Kn+1}\right) sin(\omega t) \tag{63}$$

$$\frac{u_{wall}}{U_c} \approx \left(\frac{4Kn}{4Kn+1}\right) cos(\omega t) \tag{64}$$

$$\frac{u_{wall}}{U_s} \approx \left(\frac{4Kn}{4Kn+1}\right) sin(\omega t) \tag{65}$$

3.2.2 High-Womersley Number Flows

For high-Womersley number cases, the profiles are similar to the Stokes solution of impulsively start flat-plate. The viscous effects are limited to a region of thickness δ close to the wall. The variation of boundary layer thickness with Womersley number is shown in Fig. 13. Here, the boundary layer thickness is defined as the distance away from the wall at which the velocity is 101 percent of the center velocity (see Fig. 7 (c)). Since this flow condition is satisfied at multiple locations, the location near the center is selected as δ. Here, the boundary layer thickness is proportional to the inverse of Womersley number ($\delta \propto \frac{1}{\alpha}$) as shown in Fig. 13 (a). Boundary layer thickness gets reduced with an increase in Womersley number and approaches zero as $W_o \to \infty$.

The following form of the asymptotic expansion of Bessel function (Watson (1995)) is used to calculate the limiting value of g (c, Kn,r), as $x \to \infty$

$$J_n(x) = \left(\frac{2}{\pi x}\right)^{\frac{1}{2}}[\cos(x - \frac{1}{2}n\pi - \frac{\pi}{4})] \tag{66}$$

The limiting value of the function g (c,Kn,r) is:

$$\lim_{\alpha\to\infty} g(c, Kn, r) = 1 + 0i \tag{67}$$

hence for $W_o \to \infty$, the center and wall velocity are

$$\frac{u_c}{U_c} \approx \frac{u_{r\approx R}}{U_c} = cos(\omega t) \tag{68}$$

$$\frac{u_c}{U_s} \approx \frac{u_{r\approx R}}{U_s} = sin(\omega t) \quad (69)$$

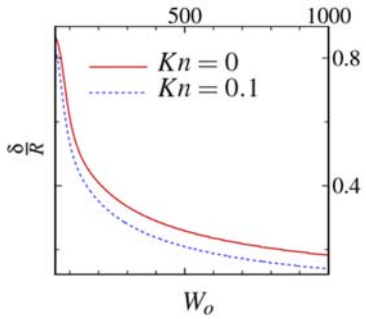

Fig. 13. Variation of boundary layer thickness with Womersley number at T = $\frac{\pi}{2}$ for sine flows.

3.3 Arbitrary Inflow: Temporal Variation of Velocity and Pressure Gradient

The evolution of velocity and pressure gradient for an arbitrary inflow and comparison with the results of Das and Arakeri (Das and Arakeri (2000)) are illustrated in Figs. 14 and 15. A trapezoidal piston motion (U_p) is represented using Fourier series as shown in Fig. 14 (a). Here, two hundred (l_{max} = 200) Fourier terms are used to represent the trapezoidal function. A closeup view of the fitted curve is shown in the inset of Fig. 14 (a). The fitted curve has large oscillations near the jump (Gibbs phenomenon). The transient variation of pressure gradient is shown in Fig. 14 (b). Because of the small mismatch between the trapezoidal and fitted curve, non-dimensional pressure gradient exhibits more oscillations near the jump.

The velocity profiles during different phases of the piston motion are shown in Figs. 15 (a) - (d). The solutions obtained during accelerating (Fig. 15 (a)), constant velocity (Fig. 15 (b)), decelerating (Fig. 15 (c)) and zero velocity (Fig. 15 (d)) phases match with the solutions of Das and Arakeri (Das and Arakeri (2000)) as shown in Figs. 14 and 15.

4. CONCLUSION

New analytical solutions with slip conditions for starting, oscillatory and arbitrary flows are obtained in terms of Bessel functions for micro-pipe flows. The scaling laws associated with starting and oscillatory flows are provided whenever possible using Knudsen, Reynolds and Womersley numbers. Effects of dimensionless numbers of friction factor, boundary layer thickness and entry-length are also examined.

Initially, the expressions for velocity profiles, pressure gradient and wall shear stress for starting flows are analyzed. The flow solution has two parts: the first part is steady and the other is the transient part. It is observed that the transient part decays at $\tau \approx 0.3$, and the flow attains a steady-state when $\tau > 0.3$. Expressions for velocity profile in terms of pressure gradient for steady flows in a manner similar to the Hagen-Poiseuille equation are obtained for pipe flows with slip boundary conditions. The solutions are compared with previously published analytical solutions. Simplified expressions for slip-length are obtained for steady conditions.

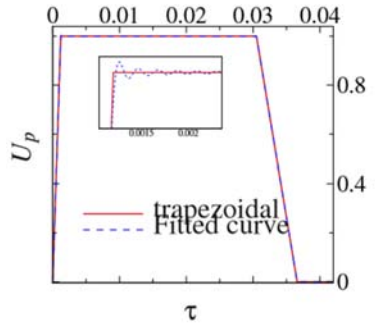

(a)

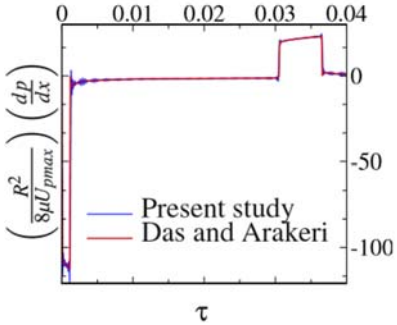

(b)

Fig. 14. Validation of analytical solution; (a) normalized piston velocity (b) Temporal variation of pressure gradient.

For oscillatory starting flow (sine/cosine flows), the solution consists of two parts: the first part is pure oscillatory and the other part is the transient decaying part. Asymptotic behavior of the solutions is obtained. A solution for the steady part of the starting flow is regained by limiting the Womersley number to zero. Flow is classified into three regions: low-Womersley number flow (I), medium Womersley number flow (II) and high-Womersley number flow (III) by quantifying the maximum velocity location. For viscous dominated low-Womersley number cases (I), the maximum velocity is always observed at the center of the geometry and a simplified series solution predicts the flow behavior. For high-Womersley number flow conditions, the viscous effects are confined near the vicinity of the solid surface. The variation of boundary layer thickness with Womersley number is analyzed. As Womersley number approaches infinity, the solutions become independent of viscosity and oscillate like a plug flow. In region III the maximum velocity location and boundary layer thickness are proportional to the inverse of Womersley number for pipe flows with slip conditions.

Finally, a more general case with an arbitrary inflow is analyzed. The solutions obtained are compared with the existing expression of velocity and pressure gradient available in the literature.

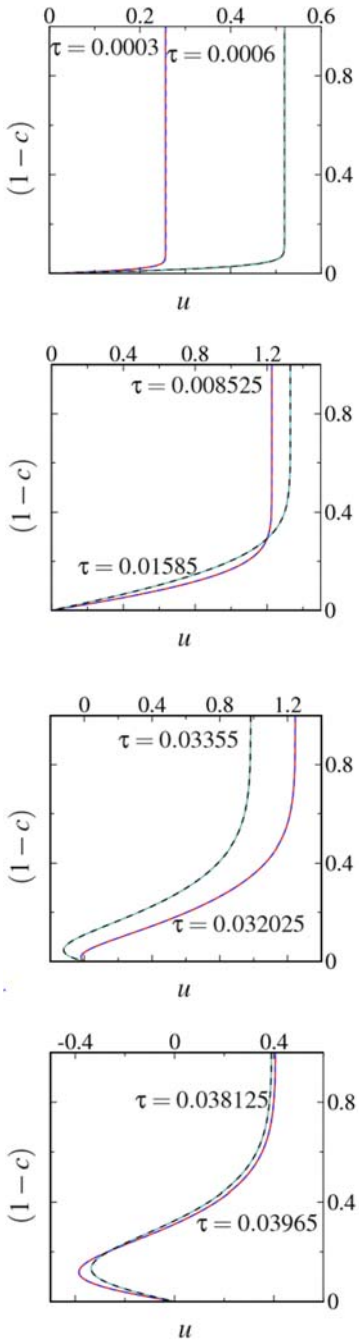

Fig. 15. Validation of analytical solution (velocity profiles); dashed line: analytical solution, solid line: (a) accelerating phase, (b) constant velocity phase, (c) decelerating phase, (d) zero velocity phase.

APPENDIX

Calculation of Inverse Laplace Transform: Starting Pipe Flows

Inverse Laplace transform is evaluated using Mellin's inverse formula (Eq. 21) together with Cauchy's Residue theorem. Taking the Laplace transform of Eq. 2 we get:

$$u_{avg}(s) = \frac{U_0}{s} \tag{70}$$

The velocity profiles are obtained by combining the residues at the poles of the integrand and given by:

$$u(r,t) = \sum \text{residues of poles of } \left(\frac{U_0}{s}\bar{\xi}(r,s)e^{St}\right) \tag{71}$$

The residue at z = z_0 for a pole of order n is given by:

$$Res|_{z=z_0} = \frac{1}{(n-1)!}\frac{d^{n-1}}{dz^{n-1}}[(z-z_0)^n f(z)]|_{z=z_0} \tag{72}$$

Using this expression, the residue at s = 0 is obtained in the following form:

$$Res_0 = 2U_0\left[\frac{(1-c^2)+2Kn}{1+4Kn}\right] \tag{73}$$

The other singular points are the zeros of

$$I_0(B\sqrt{s}) + Kn(B\sqrt{s})I_1(B\sqrt{s}) - \frac{2}{B\sqrt{s}}I_1(B\sqrt{s}) = -J_2(v) - KnvJ_1(v)$$

If ν_n are the zeros of this expression, then $s_n = -\frac{\nu_n^2}{B^2}$ are the poles. These are simple poles. For a first order pole at z = z_0 and with the function *f* written in the form f = $\frac{N(z)}{D(z)}$, the residue is $\frac{N(z_0)}{D\prime(z_0)}$. Residues at each of these poles are obtained as follows:

$$Res_n = 2U_0 e^{-\nu_n^2\tau}\mathfrak{B}(\nu, \mathrm{Kn}, \mathrm{r}) \tag{74}$$

The solution is obtained by combining the single residue (Res_0) and all the Res_n.

Calculation of Inverse Laplace Transform: Sinusoidal Sine Flows in Pipes

By taking the Laplace transform of Eq. 3 we get:

$$u_{avg}(s) = \frac{U_S\omega}{s^2+\omega^2} \tag{75}$$

Applying Cauchy's Residue theorem to Eq. 21,

$$u(r,t) = \sum \text{residues of poles of } \left(\frac{U_S\omega}{s^2+\omega^2}\bar{\xi}(r,s)e^{St}\right) \tag{76}$$

Here, s = iω and s = −iω are poles of order 1. The residue at s = iω is:

$$\mathrm{Res}_{i\omega} = \left[-\frac{iU_s}{2}e^{i\omega t}\left(\frac{J_0(cv_a)+Knv_bJ_1(v_a)-J_0(v_a)}{J_2(v_a)+Knv_bJ_1(v_a)}\right)\right] \tag{77}$$

where $iv_a = \alpha i^{\frac{1}{2}}$. Similarly, the residue at s = −iω is:

$$\mathrm{Res}_{-i\omega} = \left[\frac{iU_s}{2}e^{-i\omega t}\left(\frac{J_0(cv_b)+Knv_bJ_1(v_b)-J_0(v_b)}{J_2(v_b)+Knv_bJ_1(v_b)}\right)\right] \tag{78}$$

Where $iv_b = \alpha(-i)^{\frac{1}{2}}$. It can be proved that $\mathcal{R}(\mathrm{Res}_{i\omega}) = \mathcal{R}(\mathrm{Res}_{-i\omega})$. The other singular points are the zeros of

$$I_0(B\sqrt{s}) + Kn(B\sqrt{s})I_1(B\sqrt{s}) - \frac{2}{B\sqrt{s}}I_1(B\sqrt{s}) = -J_2(v) - KnvJ_1(v)$$

If ν_n are the zeros of this expression, then $s_n = -\frac{\nu_n^2}{B^2}$ are the poles. These are simple poles. Residues at each of these poles are obtained as follows:

$$Res_n = \frac{-2U_s\nu_n^4}{\nu_n^4+W_0^2}e^{-\nu_m^2\tau}\mathfrak{B}(\nu, \mathrm{Kn}, \mathrm{r}) \tag{79}$$

The solution is obtained by combining the residues $Res_{i\omega}$, $Res_{-i\omega}$ and all the Res_n

REFERENCES

Avramenko, A., A. Tyrinov, and I. Shevchuk (2015). An analytical and numerical study on the start-up flow of slightly rarefied gases in a parallel-plate channel and a pipe. *Physics of Fluids* 27(4), 042001.

Batchelor, G. (1967). *An introduction to fluid dynamics*. Cambridge University Press.

Brereton, G. (2000). The interdependence of friction, pressure gradient, and flow rate in unsteady laminar parallel flows. *Physics of Fluids* 12(3), 518–530.

Chen, C. I. C. K. Chen, and H. J. Lin (2008). Analysis of unsteady flow through a microtube with wall slip and given inlet volume flow rate variations. *Journal of Applied Mechanics* 75(1), 014506.

Damianou, Y., M. Philippou, G. Kaoullas, and G. C. Georgiou (2014). Cessation of viscoplastic poiseuille flow with wall slip. *Journal of Non-Newtonian Fluid Mechanics* 203, 24–37.

Das, D., and J. Arakeri (2000). Unsteady laminar duct flow with a given volume flow rate variation. *Journal of applied mechanics* 67(2), 274–281.

Durst, F., S. Ray, B. ¨Unsal, and O. Bayoumi (2005). The development lengths of laminar pipe and channel flows. *Journal of Fluids Engineering* 127(6), 1154–1160.

Hayat, T., M. F. Afzaal, C. Fetecau, and A. A. Hendi (2011). Slip effects on the oscillatory flow in a porous medium. *Journal of Porous Media* 14(6).

Hayat, T., S. Zaib, C. Fetecau, and C. Fetecau (2010). Flows in a fractional generalized burgersfluid. *Journal of Porous Media* 13(8).

Jog, C. S. (2002). *Foundations and Applications of Mechanics: Fluid Mechanics*, Volume 2. CRC Press.

Kaoullas, G., and G. C. Georgiou (2013). Slip yield stress effects in start-up newtonian poiseuille flows. *Rheologica Acta* 52(10-12), 913–925.

Kaoullas, G., and G. C. Georgiou (2015). Start- up and cessation newtonian poiseuille and couette flows with dynamic wall slip. *Meccanica* 50(7), 1747–1760.

Khaled, A. R. and K. Vafai (2004). The effect of the slip condition on stokes and couette flows due to an oscillating wall: exact solutions. *International Journal of Non-Linear Mechanics* 39(5), 795–809.

Khan, M. (2007). Partial slip effects on the oscillatory flows of a fractional jeffrey fluid in a porous medium. *Journal of Porous Media* 10(5).

Majdalani, J. (2008). Exact navier-stokes solution for the pulsatory viscous channel flow with arbitrary pressure gradient. *Journal of propulsion and power* 24(6), 1412–1423.

Muntges, D., and J. Majdalani (2002). Pulsatory channel flow for an arbitrary volumetric flowrate. *In 32nd AIAA Fluid Dynamics Conference and Exhibit*, pp. 2856.

Panton, R. L. (2013). *Incompressible flow*. John Wiley & Sons.

Ray, S., B. Ünsal, F. Durst, Ö. Ertunc, and O. Bayoumi (2005). Mass flow rate controlled fully developed laminar pulsating pipe flows. *Journal of Fluids Engineering* 127(3), 405–418.

Schlichting, H., and K. Gersten (2016). *Boundary-layer theory*. Springer.

Uchida, S. (1956). The pulsating viscous flow superposed on the steady laminar motion of incompressible fluid in a circular pipe. *Zeitschrift f ü r angewandte Mathematik und Physik ZAMP* 7(5), 403–422.

Watson, G. N. (1995). *A treatise on the theory of Bessel functions*. Cambridge University Press.

Weinbaum, S. and K. Parker (1975). The laminar decay of suddenly blocked channel and pipe flows. *Journal of Fluid Mechanics* 69(4), 729–752.

Womersley, J. R. (1955). Method for the calculation of velocity, rate of flow and viscous drag in arteries when the pressure gradient is known. *The Journal of physiology* 127(3), 553–563.